HHS Public Access

Author manuscript

Phys Chem Chem Phys. Author manuscript; available in PMC 2019 March 28.

Published in final edited form as:

Phys Chem Chem Phys. 2018 March 28; 20(12): 8166–8176. doi:10.1039/c7cp06624d.

L-edge sum rule analysis on 3d transition metal sites: from d^{10} to d^0 and towards application to extremely dilute metallo-enzymes

Hongxin Wang[1,2], **Stephan Friedrich**[3], **Lei Li**[4], **Ziliang Mao**[1], **Pinghua Ge**[5], **Mahalingam Balasubramanian**[6], and **Daulat S. Patil**[2]

[1]Department of Chemistry, University of California, Davis, CA 95616, USA

[2]Lawrence Berkeley National Laboratory, Berkeley, CA 94720, USA

[3]Lawrence Livermore National Laboratory, Advanced Detectors Group, 7000 East Avenue, Livermore, CA 94550, USA

[4]Synchrotron Radiation Nanotechnology Center, University of Hyogo, 1-490-2 Kouto, Shingu-cho, Tatsuno, Hyogo 679-5165, Japan

[5]Department of Physics, University of Illinois, 1110 West Green St., Urbana, IL 61801, USA

[6]Argonne National Laboratory, 9700 S. Cass Ave., Argonne, IL 60439, USA

Abstract

According to L-edge sum rules, the number of 3d vacancies at a transition metal site is directly proportional to the integrated intensity of the L-edge X-ray absorption spectrum (XAS) for the corresponding metal complex. In this study, the numbers of 3d holes are characterized quantitatively or semi-quantitatively for a series of manganese (Mn) and nickel (Ni) complexes, including the electron configurations $3d^{10} \rightarrow 3d^0$. In addition, extremely dilute (<0.1% wt./wt.) Ni enzymes were examined with two different approaches: 1) by using a high resolution superconducting tunnel junction (STJ) X-ray detector to obtain XAS spectra with very high signal-to-noise ratio, especially in the non-variant edge jump region; and 2) by adding an inert tracer to the sample that provides a prominent spectral feature to replace the weak edge jump for intensity normalization. In this publication, we present for the first time: 1) L-edge sum rule analysis for a series of Mn and Ni complexes that include electron configurations from an open shell $3d^0$ to a closed shell $3d^{10}$; 2) a systematic analysis on the uncertainties, especially on that from the edge jump, which was missing in all previous reports; 3) a clearly-resolved edge jump between the pre-L_3 and the post-L_2 regions from an extremely dilute sample; 4) an evaluation of an alternative normalization standard for L-edge sum rule analysis. XAS from two copper (Cu) proteins measured with a conventional semiconductor X-ray detector are also repeated as bridges between the Ni complexes and the dilute Ni enzymes. The differences between measuring 1% Cu enzymes and measuring < 0.1% Ni enzymes are compared and discussed. This study extends L-edge sum rule analysis to virtually any 3d metal complex and any dilute biological samples that contain 3d metals.

Correspondence to: Hongxin Wang.

Keywords

Integrated L-edge X-ray absorption spectroscopy; integrated L XAS; integrated K XAS; L-edge sum rule; L-edge sum rule; XAS edge jump; error analysis; 3d vacancies (holes); oxidation state; superconducting tunnel junction (STJ) X-ray detector; manganese complex; nickel complex; nickel enzyme; copper enzyme

1. Introduction

The oxidation state is an indicator of the degree of oxidation for a particular atom and is one of the most-pursued quantities in chemistry, because the distribution of electron/charge density in inorganic complexes or enzymatic metal sites determines their chemical, physical and biological functions/properties. Unlike alkali or alkaline earth metals, transition metals can have different oxidation states, and thus different chemical properties. For example, manganese (Mn) complexes[1, 2] can have possible Mn^{II} to Mn^{VII} including electron configurations from $3d^5$ to $3d^0$, nickel (Ni) complexes[3, 4] can have Ni^0 to Ni^{IV} (from $3d^{10}$ to $3d^6$), while copper complexes can have Cu^I and Cu^{II} sites. In inorganic and bioinorganic chemistry, resolved oxidation states, i.e. the measured number of electrons/holes localized in the bonding orbital, have helped understand the chemical and biochemical roles of many metal sites,[4–6] while unresolved oxidation states have contributed to longstanding controversies in many systems.[3, 7–11] The oxidation state is typically characterized by an integer, which is the hypothetical charge in an atom assuming the bonding is 100% ionic. Since a real 100% ionicity does not exist, and there is ambiguity of the assignment of the oxidation state of the electronegative ligands, metal oxidation states may be represented more quantitatively by the number of vacancies (holes) localized at the metal sites (*e.g.* Mn or Ni).[4]

X-ray absorption spectroscopy (XAS), especially L-edge XAS (or L XAS), is one of the best methods to investigate the oxidation states of 3d transition metals via absorption edge positions as well as their spectral features.[12,4, 13] In an L XAS, the L_3 edge's centroid energies, the branching ratios of $I_{L3}/(I_{L2}+I_{L3})$, and the rich multiplet structures are all sensitive to electronic structures.[4, 14–16] For example, L XAS exhibit about 2 eV per oxidation state change (eV/oxi) for the Mn complexes and 0.9 eV/oxi for Ni complexes. L-edge centroids will often be sufficient to assign oxidation states.[4,34–36] For Mn complexes, the branching ratio has also been used to determine the Mn oxidation states.[1, 17] Nevertheless, the shifts in L_3 centroids are also affected by the changes in the final state in addition to the differences in the ground states. The spectral multiplets and branching ratios are also sensitive to metal's electronic spin states and its coordination geometries, in addition to their oxidation states.

Sum rules link the integrated XAS absorption intensity to the number of holes localized in the X-ray absorbing metal.[4, 18] For 3d metals, L-edge XAS probes electronic transitions at 2p→3d, 2p→4s, and 2p→continuum, as shown in Fig. 1 (middle panel). A typical L-edge XAS spectrum therefore has a pair of strong absorption peaks corresponding to $2p_{3/2}$→3d and $2p_{1/2}$→3d transitions (2p→4s is 20-fold weaker) and an invariant edge jump step between the pre-L_3 and post-L_2 regions corresponding to 2p→continuum transitions.

Therefore the total number of 3d holes localized in the X-ray absorber is proportional to the integrated $L_{2,3}$-edge peaks ($2p_{1/2,\ 3/2} \rightarrow 3d$) intensity when normalized to this invariant edge jump, as reported previously.[4–6, 19–21] Besides being able to obtain a number of 3d holes (H_{3d}), the integrated L intensity I_L is a pure ground state property and is well-suited for investigating d-shell vacancies.[4] In the past, L-edge sum rule analysis has been applied to one set of Ni[4] and one set of Cu[5, 6] model complexes, and a few Cu proteins with Cu concentrations of order ~1% wt./wt.[5, 6] However, the error bars for their XAS (especially for the weak edge jump) were not well-discussed or controlled. In addition, L-edge sum rule analysis on Mn or other 3d metal complexes and on samples with < 0.1% wt./wt. metal concentration are not available.

In this publication, we first characterize a series of Mn and Ni complexes with L-edge sum rule analysis. We then extend this analysis to NiFe hydrogenase (H_2ase) and CO-dehydrogenase (CODH), which have an extremely dilute Ni concentration of < 0.1% wt./wt. Two approaches to make this extension available are discussed. The differences between measuring 1% Cu enzymes and measuring < 0.1% Ni enzymes are also addressed. For the first time, we present: 1) L-edge sum rule analysis on a series of 3d metal complexes, which include electron configurations from an open shell $3d^0$ to a closed shell $3d^{10}$; 2) a systematic analysis of the error bars for L-edge XAS, especially for their edge jump regions; 3) a clearly-resolved edge jump between the pre-L_3 and the post-L_2 regions for an extremely dilute sample (< 0.1% Ni); and 4) a detailed evaluation on using an alternative normalization standard for L-edge sum rule analysis.

2. Experimental section

Samples

$Ni^{II}F_2$, $Ni^{II}Cl_2$, $Ni^{II}Br_2$, $Ni^{II}O$, $Ni^{II}(OH)_2$, $Mn^{II}O$, $LiMn^{III}O_2$, $Mn_2^{IV}O_3$, $Mn^{IV}O_2$, and $KMn^{VII}O_4$ were purchased from Sigma-Aldrich, stored in desiccator and used without further treatment. Ionic $K_3Ni^{III}F_6$ complex[22] and $LiNiO_2$, Ni_2O_3, $KNi^{IV}IO_6$[23, 24] were provided by Dr. Neil Bartlett from UC Berkeley and Dr. Melendres from Argonne National Lab respectively. Covalent Ni-S complexes $Na_2[Ni^0(SR)_4]$, $Na[Ni^I(SR)_4]$, $[Ni^{II}(SR)_4]$, where $(SR)_4$ = bis(diphenylbis((methylthio)methyl)borate and $[PhTt^{tBu}]Ni^ICO$, $[PhTt^{tBu}]Ni^{II}(Cl)$, where $PhTt^{tBu}$ = phenyltris((*tert*-butylthio)methyl)borate,[25, 26] were prepared in Dr. Charles Riordan's group from the University of Delaware. All solid model complexes were finely ground and pressed onto a piece of UHV compatible carbon tape inside a nitrogen (N_2) atmosphere glovebox (although not all the samples are air sensitive). Such prepared samples were loaded into the UHV measurement chamber with a vacuum loadlock.

Blue Cu protein from the construct engineered *azurin* and from *plastocyanin* were prepared[5, 27–29] by Professor E.I. Solomon's laboratory at Stanford University. They were used as examples of metalloenzymes with moderate metal concentration (*e.g* ~1% Cu, wt./wt.). *Clostridium thermoaceticum*-CODH (or *Ct*-CODH) was purified and prepared[30, 31] in Dr. P. W. Ludden's laboratory. The 310 kDa tetramer has four Ni sites, corresponding to about 770 ppm (or 0.077%) Ni concentration. The as-isolated and H_2 reduced NiFe H_2ase solution samples (< 0.067% wt./wt.) were prepared from *D. gigas* H_2ase[12, 32, 33] at

Lawrence Berkeley National Laboratory. The two Ni enzymes were examples of extremely dilute samples with < 0.1% metal concentration. For most enzyme samples, partially dehydrated films were made by drying the solution samples on sapphire substrates under a H_2 atmosphere (for the H_2 reduced NiFe H_2ase sample) or a N_2 atmosphere (for other samples). For *Ct-CODH* enzyme, a frozen solution sample was prepared instead of partially dehydrated films.

The Ce M_5 edge at 881.7 eV is close to Ni L_3 edge at 852.6 eV and can be used as an intensity normalization standard in the Ni L-edge sum rule analysis instead of the more commonly used edge jump. To establish the method, a testing complex mixture was first prepared and evaluated. Inside the glovebox, 0.1M $NiBr_2$-TRIS-HCl solution was prepared, providing a sample with ~ 0.6% Ni concentration (wt./wt). The $Ce(NO_3)_3$•$6H_2O$ (or $Ce(NO_3)_3$ for short) was then added to the 0.1M solution. Due to the extremely short penetration depth by soft X-rays (0.5 μm in H_2O and ~200Å in typical solids), the Ni, Ce and buffer mixture must be homogenized on a microscopic scale in solution. Experimentally, the best molar ratio for $NiBr_2$:$Ce(NO_3)_3$ was found to be ~ 1:5.5, when compatible signal intensities for Ni L_3 and for Ce M_5 edges were obtained in the XAS spectra. For NiFe H_2ase, $Ce(NO_3)_3$ was added to the as-isolated enzyme solution. The H_2-reduced solution was then prepared by incubating the as-isolated H_2ase with added $Ce(NO_3)_3$ under pure H_2 for >8 hours. This maintains a constant Ni:Ce ratio in the as-isolated and the reduced samples, although their absolute concentration may be different.

XAS Measurements

L-edge XAS was measured at Stanford Synchrotron Radiation Laboratory (SSRL) beamline 8–2[34] and at Advanced Light Source (ALS) beamline 9.3.2[35] and 4.0.2[36] inside a UHV chamber under windowless operation.[13, 37] These beamlines have an energy resolution of 1.0 eV, 0.4 eV and 0.2 eV, respectively, at the Ni L-edge at 850 eV. For concentrated Mn and Ni complexes, the XAS spectra were measured by total electron yield (TEY)[15] using a Galileo 4716 channeltron electron multiplier as photoelectron detector. The incident beam intensity (I_0) was monitored through a gold-plated grid. For biological samples or dilute $NiBr_2$ matrix samples, XAS were measured by partial X-ray fluorescence yield (PFY)[12, 31] using a 30-element germanium (Ge) array detector with 180 eV energy resolution, or a 9- or 36-element superconducting tunnel junction (STJ) detector with 15 eV energy resolution.[39,40] For measuring < 0.1% Ni *Ct*-CODH, the use of an STJ detector was necessary to extract the weak Ni signal from the high spectral background. During these measurements, one region was defined around Ni L, Cu L or Ce M partial fluorescence signal (PF), which is proportional to the metal absorbance and incident X-ray beam intensity, while the second region was set at around the oxygen (O) K fluorescence signal used as a measure of I_0.

Superconducting tunnel junctions (STJs)[38–41] are high-resolution X-ray detectors that consist of two superconducting electrodes separated by an extremely thin layer of insulating material. Electric current can pass through the STJ junction via the quantum-mechanical tunneling effect. X-rays absorbed in one of the electrodes will generate free excess charges in proportion to the X-ray energy, and the subsequent increase in tunneling current can be directly read out with a room temperature amplifier. STJ X-ray detectors exploit the

extremely small (~1 meV) energy gap in superconductors to achieve an order of magnitude higher energy resolution than conventional semiconductor detectors, which have an energy gap of ~1 eV. In general, our Nb-based STJ detector has a 10–20 eV energy resolution[39, 42, 43] while a semiconductor detector has 100–300 eV[38, 44, 45]. The higher energy resolution allows a more effective rejection of unwanted background counts and increases the signal-to-noise ratio (S/N) for the L- and M-edge PFY XAS spectra for dilute samples.[39, 42, 43] This is especially true for resolving the weak features, such as the edge jump steps.

For the measurements at SSRL, each concentrated Ni complex spectrum was the sum of 5–6 raw scans, each blue Cu protein spectrum was the sum of 20 scans, while each NiFe H_2ase spectrum represented the sum of 40 raw scans. The Ni complexes were measured at room temperature, while the blue Cu enzymes and NiFe H_2ases were measured at 10K maintained with a liquid helium flow cryostat. At ALS, each Mn complex spectrum was the sum of 3–5 raw scans, each dilute $NiBr_2$ spectrum was the sum of 6 raw scans, while each *Ct*-CODH spectrum represented the sum of 10 raw scans. The energies were calibrated with MnO at 638.7 eV, NiF_2 at 852.7 eV, and CuO at 932.7 eV for the respective samples.[46] As the beam intensity is much stronger at ALS in comparison with that at SSRL, all the spectra were recorded at 10K (using a LHe cryostat). To further minimize the possible radiation damage and photoreduction, the position of the X-ray beam on the sample was moved for every scan. We also tested multiple short scans at one spot for all the samples at the ALS and at SSRL, but observed no spectral change under our experimental conditions.

The L-edge data processing for complex samples involves subtraction of the spectral background, using their sample holders XAS as reference (as will be addressed in detail in the Error Analysis section). These L XAS spectra were then normalized to the invariant edge jump between the pre-L_3 and the post-L_2 regions to produce the integrated L-edge spectra. The non-resonant edge jumps were then removed by subtracting a simulated two-step function. The L_3 and L_2 intensities (I_{L3} and I_{L2}) were obtained from these spectra by integration over 929–936 and 950–955 eV for Cu proteins, over 851–858 and 868–875 eV for Ni samples, and over 634.2–657.6 eV for Mn complexes. For STJ measured *Ct*-CODH XAS, a process similar to the one for processing Ni complex data was used to calculate I_{L3} and I_{L2}. For the NiFe H_2ase and the dilute $NiBr_2$ XAS, the integrated Ce M_5-edge intensity was used as an alternative intensity normalization standard, because these spectra do not exhibit an observable edge jump.

K-edge XAS for MnO, Mn_2O_3 and $KMnO_4$ were measured at BL08B2 of the SPring-8 synchrotron radiation facility in Hyogo Prefecture, Japan. The main X-ray optical elements consist of a first Rh-coated vertical collimation mirror, a double-crystal monochromator and a second Rh-coated vertical refocusing mirror. A water-cooled Si (111) double-crystal monochromator was used to produce a ~1 eV bandwidth X-ray beam with a beam size of 2.0 mm in the horizontal direction and 0.5 mm in the vertical direction. The K-edge XAS data were measured in transmission mode over an energy range from −330 to 1500 eV with respect to the Mn absorption edge by using ionization chambers to record the incoming and transmitted intensities. The transmission measurement is possible because Mn K-edge has a transmission depth of ~1 mm. The Mn K absorption edge was defined as the first peak in the

first derivative spectrum of XAS data. A Mn foil with an XAS absorption edge at 6539 eV was used as the energy calibration standard for the monochromators.

3. Results and discussions

Five published Ni XAS spectra[4] were either re-measured (on NiF_2, K_3NiF_6 and $KNiIO_6$) or cited (for $[Ni^{I/II}(SR)_4]^{-/0}$) and compared with the XAS for five new Ni and five additional Mn complexes. The errors for all fifteen L-edge XAS spectra were evaluated or re-evaluated with the new method.

XAS Spectra of Ni and Mn Complexes

Examples of the observed Ni and Mn L-edge spectra are shown in Fig. 1, with Ni complexes from d^{10} to d^6 in the left panel and Mn complexes from d^5 to d^0 in the right panel. Since $[Ni^0(SR)_4]^{2-}$ has a closed $3d^{10}$ shell, its 2p→3d resonance intensity should be absent, and this is indeed the case (Fig 1a, dashed red line). The L-edge XAS spectrum is then dominated by the 2p→continuum transition, also called the edge jump. This edge jump does not change with the number of 3d holes and can therefore be used to normalize XAS spectra. All spectra in Fig. 1 were normalized to their corresponding edge jumps between the pre-L_3 and post-L_2 regions. Although $[Ni^0(SR)_4]^{2-}$ may not be an interesting compound in synthetic chemistry, it did provide us with the first L-edge XAS for a real d^{10} sample, which is rare. We emphasize that although Ni metal is also nominally Ni^0, it has an electronic configuration of $3d^84s^2$ rather than $3d^{10}$, and a typical Ni^{II} L-XAS feature as shown in Fig. S1 in the supplemental information (SI).

In contrast, $[Ni^I(SR)_4]^-$ has a $3d^9$ configuration, opening up one d hole for obvious $2p_{3/2}$→3d and $2p_{1/2}$→3d resonant transitions (Fig. 1a, solid black line). As the oxidation state further increases to Ni^{II}, Ni^{III}, and Ni^{IV}, the number of d-holes increases gradually, and so does the L-edge resonance intensity (Fig. 1a→1d).[4]

In the right panel, although the d^5 MnO_2 has the smallest intensity among the Mn complexes, it still has higher L_3 and L_2 intensities than the highest Ni intensity (for $KNi^{IV}IO_6$). As the Mn oxidation state continues to increase (d^5→d^4→d^3→d^0 in Fig. 1e→1h), the L-edge resonance intensity also increases significantly as expected. In addition to the integrated intensities, these Ni and Mn spectra contain additional information, such as L_3 centroid energies, branching ratios of $I_{L3}/(I_{L2}+I_{L3})$, and multiplet structures.[4, 14–16] Nevertheless, as mentioned in the introduction, only integrated L intensity is a pure ground state property.

L-edge sum rule

With the L-edge XAS spectra normalized to the invariant edge jump, the integrated L-edge absorption intensities I_L for our Ni and Mn complexes are listed as in Table-1 and shown as in Fig. 2a. For example, we observe 0 for $[Ni^0(SR)_4]^{2-}$ (d^{10}), 14.7 for $Ni^{II}O$ (d^8), 29.4 for $KNi^{IV}IO_6$ (d^6), 36.8 for $Mn^{II}O$ (d^5), 40.9 for $Mn^{III}{}_2O_3$ (d^4), and 59.6 for $KMn^{VII}O_4$ (d^0). Here we did not attempt to evaluate the trace amount "resonant" intensity for $[Ni^0(SR)_4]^{2-}$ but simply set it to zero. There is a roughly linear dependence between the integrated L-edge intensity (I_L) and the nominal number of 3d holes (N_{3d}) as expected. The slope, which we

call R, shows an averaged normalized intensity per nominal 3d hole of about R = 6.9 in Fig. 2a. Each individual data point has an errorbar, which will be discussed in the next section.

In Fig. 2a and 2b, some additional trends are worth noticing: 1) S and N based covalent Ni complexes have obviously lower R values in comparison with O and F based ionic complexes, because the S, N have lower ionicity than the more electronegative O and F; 2) For the complexes with the same ligand donor (*e.g.* O), the L intensity per nominal 3d hole (R value) decreases as the number of nominal 3d holes increases. This again is consistent with the lower expected ionicity for higher-valence complexes; 3) Comparison of F vs. Cl and Br complexes show $R_F > R_{Cl} > R_{Br}$ as well (Table-1). This is caused by different negativities of the different ligands[47].

To convert the measured I_L to the numbers of actual 3d holes (H_{3d}, not nominal N_{3d}) on a calibrated absolute scale, we use standard samples for which the real numbers of 3d holes (H_{3d}) and their L XAS intensities (I_L) are accurately known[4]. In this study, we have: 1) Ni metal, which has an I_L = 13.1±0.7 with a band structure calculated H_{3d} = 1.5±0.1 per Ni atom[16,48,49]; 2) NiO, for which we measure I_L = 14.7, with an estimated Ni H_{3d} = 1.72 from references.[50, 51] With these two standards, the integrated L-edge intensity per 3d hole for the calibration samples is obtained as R_{cal} = 8.6. The average ionicity for our Ni and Mn complexes is therefore R/R_{cal} = 6.9/8.6 ≈ 80%.

Error Analysis

If I_L represents the L-edge peak integral and J represents the edge jump height, we can define the normalized integrated L intensity as $\alpha = I_L/J$. Then the error for this normalized intensity is given by:

$$\delta\alpha/\alpha = [(\delta I_L/I_L)^2 + (\delta J/J)^2]^{1/2} \quad (1)$$

or

$$\delta\alpha = (I_L/J)[(\delta I_L/I_L)^2 + (\delta J/J)^2]^{1/2} \quad (2)$$

Note that both $\delta I_L/I_L$ and $\delta J/J$ contribute to $\delta\alpha$. The δI_L is primarily from the integral's statistical error and the uncertainty in the choice of the integration range, while δJ is due to the uncertainty in judging the height of the edge jump. As shown in the Table-1, $\delta I_L/I_L$ varies between ±2.5% and ±5.0%. The relatively small uncertainty δI_L is consistent with the fact that I_L is an integrated value, which has an averaging effect. On the other hand, $\delta J/J$ is larger and varies between ±9.0 and ±11.8%. As illustrated in Fig. 3, the higher $\delta J/J$ is due to the shape of the spectral baseline (especially its tilt angle) in the edge jump region, which can be difficult to define and therefore increases the uncertainty in δJ. As it dominates the uncertainty of $\delta\alpha$, δJ or $\delta J/J$ must be evaluated carefully. However, the errors for $\delta\alpha$ in most previous publications included only the statistical errors of δI_L plus 10% "instrumental error",[45, 6] without any consideration of δJ.

To estimate the error δJ, we demonstrate the data processing for the L-edge sum rule analysis as in Fig. 3, which includes the removal of a spectral background to produce an intermediate XAS spectrum with a linear background (b, black) and the subsequent removal of this linear background to produce the final spectrum (c). Although the blank sample holder spectrum was measured every time, the real XAS background used in the data process is often its manipulation (tilt or bend) or simply a theoretical polynomial (a, dashed black line). In short, the initial background is just the fit of the XAS spectra in the non-resonance regions. The choice of the tilted background slope introduces a major error to δJ, with two extreme cases for NiO shown in Fig. 3 (b, red and blue spectra), although the judgement on edge jump step's height may also bring in a minor error. The difference between the slopes for the two background lines is about 25%, while the difference in the peak heights for the two "final" NiO spectra (c) is about 20%. The final value for δJ/J is ± 9.9%, while its $\delta I_L/I_L$ is ±3.4%. The $\delta I_L/I_L$ and δJ/J for other complexes are listed in Table-1. According to equation (1), δα/α is about ±10.5% for NiO and ±9.7% – ±11.7% for other complexes. These errors are presented in Table-1 and Fig.2. Most of the "instrumental error" is actually calibratable while the rest random error should already be included in our statistical error of the data, therefore we do not need to add an arbitrary 10% instrumental error to the analysis.

When the number of 3d holes is small, the above approach (with $\delta\alpha/\alpha \sim \pm 0.11$) is still accurate enough to at least semi-quantitatively identify the metal's oxidation state and its number of 3d holes (H_{3d}). For example, nominal-d^8 $[Ni^{II}(SR)_4]$ has an observed H_{3d} ~ 1.30–1.62 (1.46±0.16), which is clearly higher than d^9 $[Ni^{I}(SR)_4]^-$ (0.59–0.73); similarly, d^7 $K_3Ni^{III}F_6$ has a H_{3d} ~ 2.49–3.11, which is also significantly higher than d^8 $Ni^{II}F_2$ (1.53–1.89). This is true even for some ultra-covalent complexes which have very small difference between different oxidation states. For example, derived from I_L=8.69, 11.33, 13.25,[52] the 38–50% covalent $(Ph_4As)_2Ni[S_2C2(CF_3)_2]_2$, $(Bu_4N)Ni[S_2C_2(CF_3)_2]_2$, and $Ni[S_2C_2(CF_3)_2]_2$ complexes have distinguishable (meaning difference > δα defined by $\delta\alpha/\alpha \sim \pm 0.11$) H_{3d}=1.01, 1.32 and 1.54. Their reported L XAS[52] are cited as in Fig. S2 in SI for a reference.

However, as α increases, the observed H_{3d} values for the two consecutive oxidation states can overlap if error-bars are included. Thus a clear assignment of the oxidation state is less obvious. For example, as shown in Table 1, the d^4 $Mn^{III}_2O_3$ has a α value of 40.89±4.78, ranging from 36.11 to 45.67, while d^3 $Mn^{IV}O_2$ has 44.78±4.77 (from 40.01 to 49.55) which is overlap with the α region for d^4 $Mn^{III}_2O_3$. Under these circumstances, one has to either improve the XAS to reduce uncertainties in the edge jump δJ, or to search for alternative features in the XAS as a normalization standard for I_L. These approaches are the central topic of this publication, and we will discuss them with the L-edge sum rule analysis for dilute samples in the following sections.

Dilute Samples

For concentrated samples, the absorption features from the element of interest dominate the XAS, like those in Fig. 1. X-ray absorption of other elements such as C, N and O still contributes to the spectra as background, but their spectral features tend to be much smaller

than those from the metal of interest. For dilute samples whose metal signal is weak, most spectral counts and features are due to the large background rather than due to the metal of interest. These background intensities (B) also contributes significant statistical noise $\delta B \sim B^{1/2}$ to both I_L and J, which increases the uncertainty of α to the point that accurate analysis eventually becomes impossible. This background problem for dilute samples can be resolved by using only the X-ray fluorescence from the element of interest as a measure of absorption in XAS, instead of using the total electron yield. If the fluorescence from the element of interest can be separated efficiently from the huge background fluorescence after X-ray excitation, the XAS detection limit can be improved significantly.

A metal concentration of ~ 1% is the highest concentration for L XAS with fluorescence detection before saturation effects start to distort the spectra.[53] Therefore blue copper proteins, which have a Cu concentration ~ 1% wt./wt.,[5, 54] represent the most favorable candidates for L XAS and L-edge sum rule studies.[5, 556] In this publication, we repeated Cu L-edge sum rule analysis on the blue Cu enzymes from *plastocyanin* (Fig. 4 insert i1)[5] and from the construct engineered *azurin* (b or i2)[6] with a Ge X-ray fluorescence detector and use them as bridges between the concentrated Ni complexes and the <0.1% Ni enzymes. Our spectra reveal a H_{3d} = 0.4 (i1) and 0.2 (i2) per Cu atom, respectively.

Measuring <0.1% Ni Enzymes Using A STJ detector

CODH catalyzes CO oxidation and acetyl-CoA synthesis. It is found in acetogenic, methanogenic, and sulfate-reducing bacteria, and fixes carbon on a global scale.[56] The *Ct*-CODH has a Ni concentration of 770 ppm, only 1/13 of the Cu concentration in blue Cu proteins, which complicates L XAS and L-edge sum rule analysis. In frozen solution samples, the Ni concentration is further reduced. Fig. 4(b) illustrates an idealized fluorescence signal for a hypothetical sample with 0.077% Ni, 1.0% Cu and O in balance, assuming negligible background from pile-up or second order excitation (the detector's electronic background). While it is fine to resolve the 1% Cu signal with a 180 eV resolution Ge detector (Fig. 4a, orange), it is harder to resolve a signal from <0.1% Ni with the same detector and the same procedure (Fig. 4a, blue), even without any additional background. A lower metal concentration and a Ni X-ray energy of 850 eV (closer to the O background fluorescence) make the resolution of a <0.1% Ni signal difficult, let alone the resolution of its weak edge jump step J for L-edge sum rule analysis. With a 180 eV resolution Ge detector, the edge jump is often washed out or buried under the huge background and pile-up from light elements like C, N, O and Na.[12, 3157, 58]

STJ detectors have an energy resolution of ~15 eV instead of 180 eV. Measuring XAS with an STJ therefore produces a high resolution X-ray fluorescence spectrum, in which the hypothetical 0.077% Ni signal becomes clearly resolvable from the huge O background (Fig. 4b). In Fig. 5, the STJ measured $L_{2,3}$ XAS of *Ct*-CODH (<0.077% Ni, green) is compared to the channeltron measured XAS for the concentrated covalent $[Ni^{II}(SR)_4]$ complex (red), both spectra show a clear low spin Ni^{II} feature and both have a clear edge jump J. The L-edge sum rule analysis leads to a $\alpha = I_L/J = 12.2$ and a $H_{3d} = 12.2/8.6 = 1.42$, corresponding to a typical Ni^{II} site. With STJ detectors, L-edge sum rule analysis can readily be extended to samples with a Ni concentration <0.1%, such as *Ct*-CODH frozen solution (<0.077% Ni),

because its edge jump can be clearly observed. The same procedure will also be useful in studying other Ni enzymes with a Ni concentration below 0.1%, such as Ni in NiFe H_2ases. The advantage of this measurement is that it keeps the same ratio of normalized L intensity α and hole density H_{3d} for different measurements or for different samples. On the other hand, the disadvantage is: this approach will become difficult when H_{3d} is large (*e.g.* for Mn) because a perfect edge jump is almost impossible to obtain even with STJ detectors and a less perfect edge jump will introduce too much noise to the $\Delta\alpha$ and ΔH_{3d} because $\Delta\alpha$ (ΔH_{3d}) is large.

Measuring < 0.1% Ni Enzymes with Alternative Standard

Alternatively, we can introduce an external feature S to the XAS with its integrated intensity I_S comparable to I_L and use it as the intensity normalization standard instead of using J. For example, as Ce has a M_5 edge at 881.7 eV (close to Ni $L_{2,3}$ at 852.6 eV), we add chemically inert $Ce(NO_3)_3$ to the samples to be measured and use the Ce M_5 edge (I_S) as the normalization standard for Ni $L_{2,3}$. In this case we define $\alpha' = I_L/I_S$. This was first tested on a $NiBr_2/Ce(NO_3)_3$/buffer matrix with a 0.6% Ni concentration, as detailed in the experimental section. Compatible XAS intensities for Ni L_3 and for Ce M_5 edges were obtained for a molar ratio of $NiBr_2$:$Ce(NO_3)_3$ = 5.5:1 (Fig. 6a). The advantages of this procedure includes: one can still use a Ge detector with 180 eV resolution because it can resolve the Ni L and Ce M_5 peaks from the background; and one can have a minimum errorbar for $\delta\alpha'/\alpha'$. For the 0.6% $NiBr_2$ sample, the uncertainty $\delta I_L/I_L$ is about 4%, while the uncertainty of the Ce M_5 $\delta I_S/I_S$ is about 4.1%, leading to a total error of ~5.7% for α', much smaller than when using J for normalization. This minimized $\delta\alpha'$ increases the accuracy of the intensity ratio $\alpha' = I_L/I_S$. Note that I_L/I_S depends on the accurate knowledge of the Ni:Ce concentration ratio in a sample, and can therefore be different in different samples because the Ce concentration can vary. That complicates extracting an absolute value for the hole density H_{3d} from $\alpha' = I_L/I_S$ directly and makes this approach less attractive in comparison with the STJ option.

Nevertheless, it successfully opens another pathway to extend L-edge sum rule analysis to <0.1% Ni enzymes, such as H_2ases (0.067% Ni)[12]. These enzymes catalyze the reversible reaction of hydrogen (H_2) production and consumption, and monitoring their Ni oxidation states in their catalytic circle[8, 12, 59–61] is critical to understanding their catalytic mechanisms. As discussed in the experimental section, we added $Ce(NO_3)_3$ as intensity normalization standard S in the as-isolated sample before the H_2-reduction, both H_2ase samples therefore have the same Ce:Ni ratio, although their absolute metal concentration may be different. We obtained I_L/I_S values of 0.92 and 0.66 (Fig. 6b), leading to a ratio of 0.92/0.66=1.39 between them. This number of 1.39 is independent of the Ce concentration and is consistent with a $Ni^{III} \rightarrow Ni^{II}$ reduction for these two H_2ase samples studied[12, 59, 60]. This approach should also be a good way to study dilute systems with higher H_{3d}, such as Mn sites.

Besides Ce, a series of potential intensity standards in the spectral region from 600 to 1000 eV are also shown in the top inset of Fig. 6. For example, the Cs M_5-edge at 726 eV is a good candidate as an intensity standard for Fe $L_{2,3}$-edges at 706 and 720 eV. In addition, to

avoid the uncertain concentration ratio of Ce:Ni, some intrinsic elements in the enzymes can also be used as a standard. For example, the as-isolated *D. gigas* NiFe H_2ase contains 12 Fe (66 3d holes) and 1 Ni atoms (3 3d holes). In principle, both Fe and Ni could have a charge change when the H_2ase oxidation state varies by ±1. However, even if we assume all the ±1 change occur in Fe, its total number of 3d holes should only change 1/66=1.5%. Fe can therefore be treated as a constant and be used as a normalization standard for L-edge sum rule analysis for Ni. In this special case, the Fe and Ni concentrations will always be the same for any given protein samples (*e.g. D. gigas* NiFe H_2ase).

Comparison with K-edge XAS

L-edge XAS and K-edge XAS offer complementary advantages. For example, K-edge XAS is bulky sensitive, and the edge energies of different elements are widely spaced, which allows XAS be extended to the useful EXAFS region (Fig. S3).[62] In addition, since K X-rays have higher energies than L X-rays, K-edge XAS does not require a vacuum chamber, and a higher fluorescence yield which enables the analysis of more dilute samples.

On the other hand, L XAS has richer spectral features that provide a finger print of the sample's electronic structure. L-edges also have a much narrower line widths than K-edges (0.2 eV vs. 1 eV) that allow measuring these spectral features. For sum rule analysis, L XAS is favored over K XAS because L XAS measures 2p→3d transitions and therefore provides direct information about 3d bonding orbitals. These transitions are dipole allowed and therefore much stronger and more stable than the pre-K 1s→3d. As illustrated in Fig. 7, the maximum 1s→3d feature in K XAS (Fig. 7a, black) is still smaller than its edge jump, while most of the 1s→3d features are barely visible (Fig. 7a, green and red). Meanwhile, L XAS has a signal size several times stronger than its corresponding edge jump and 10–500 times stronger than the corresponding 1s→3d features in K XAS, because 2p→3d transitions are dipole allowed but 1s→3d is not. Moreover, as 1s→3d is not dipole allowed, the weak feature's intensity heavily depends on the extent of its orbital mixture with other dipole allowed transitions and thus on the geometric structures of the complex. This also makes 1s→3d transitions dependent on changes in the electronic structure and difficult to interpret. For example, according to the L-edge sum rule analysis, H_{3d} for MnO should be about 60% of that for $KMnO_4$. However, this ratio is only a few percent in K-edge XAS (Figure 6a, green vs. black), and $Mn^{III}O_3$ actually has slightly lower intensity than $Mn^{II}O$ in K-edge XAS.

4. Summary

According to sum rules, the integrated L XAS intensity I_L (when normalized by the invariant edge jump J) is proportional to the number of 3d holes localized in the X-ray absorber (H_{3d}). We have used L-edge sum rules to obtain the H_{3d} from their corresponding I_L/J for a series of Ni and Mn complexes ($3d^{10}$→$3d^0$). In complementary to the previous reports, errors in estimating the edge jump (δJ) are identified as dominant and must be carefully controlled. When the number of 3d holes is small, the I_L/J approach is accurate enough to at least semi-quantitatively define the metal's oxidation state. However, as I_L/J increases, the H_{3d} observed values for the two consecutive oxidation states can overlap and a clear assignment

of the oxidation state is less obvious. In this case, one has to either improve the accuracy of the setup and measure XAS with a clearer edge jump J (with a smaller error δJ), or to use alternative spectral features I_S to normalize I_L.

We have examined these two approaches to measure and extended the method to studies of extremely dilute biological samples (<0.1% Ni), such as *Ct*-CODH and NiFe H_2ase. For higher-accuracy XAS, we use a ~15 eV high resolution STJ detector to separate the extremely weak Ni fluorescence from the huge background to obtain the edge jump J with high signal-to-noise ratio, and continue to use the L-edge sum rule procedure developed for Ni complexes. The STJ measured L XAS for *Ct*-CODH (< 0.077% Ni) illustrates this option and conclude it has a Ni^{II} site. As an alternative spectral feature, we have added inert Ce to our samples and use the Ce M_5 as the new intensity normalization standard for I_L. This reduces the total error in $\alpha = I_L/I_S$, as demonstrated with a dilute $NiBr_2$ (0.6% Ni) samples and with NiFe H_2ase samples (0.067% Ni). Although this analysis depends on the Ce concentration, changes in oxidation state for a given sample do not change the Ni:Ce ratio. This is shown in the comparison of as-isolated and H_2-reduced NiFe H_2ase samples, whose ratio of 1.39 is consistent with a $Ni^{III} \rightarrow Ni^{II}$ reduction. These experimental approaches will enable us to extend L-edge sum rule analysis to virtually any dilute biological metals in the future.

Supplementary Material

Refer to Web version on PubMed Central for supplementary material.

Acknowledgments

We thank Professor Stephen P. Cramer at UC Davis and at Lawrence Berkeley National Lab for providing the laboratory and beamline facilities for the experiments, which were supported by NIH grant GM-65440. We also thank our former colleague Dr. Robert Johns for preparing dilute $NiBr_2$, and Dr. Neil Bartlett at UC Berkeley, Dr. Melendres at Argonne National Lab and Dr. Riordan at the University of Delaware for providing non-commercial samples. Stanford Synchrotron Radiation Laboratory and Advanced Light Source are supported by the Department of Energy, Office of Basic Energy Sciences. This research is also part of the advanced biological experimental X-ray spectroscopy program (ABEX), which is supported by the U.S. Department of Energy, Office of Biological and Environmental Research. The Mn K-edge XAS experiments were performed at the beamline BL08B2 of SPring-8 with the approval of the Japan Synchrotron Radiation Research Institute (JASRI) (Proposal Nos. 2016B3302 and 2017A3302). Part of this work was performed under the auspices of the U.S. Department of Energy by Lawrence Livermore National Laboratory under Contract DE-AC52-07NA27344.

References

1. Peng G, Degroot FMF, Hämäläinen K, Moore JA, Wang X, Grush MM, Hastings JB, Siddons DP, Armstrong WH, Mullins OC, Cramer SP. Journal of the American Chemical Society. 1994; 116:2914–2920.
2. Visser H, Anxolabehere-Mallart E, Bergmann U, Glatzel P, Robblee JH, Cramer SP, Girerd J-J, Cinco RM, Sauer K, Klein MP, Yachandra VK. Journal of the American Chemical Society. 2001; 123:7031–7039. [PubMed: 11459481]
3. Lippard, SJ., Berg, JM. Principles of Bioinorganic Chemistry. University Science Books; Mill Valley, CA: 1994.
4. Wang HX, Ge PH, Riordan CG, Brooker S, Woomer CG, Collins T, Melendres CA, Graudejus O, Bartlett N, Cramer SP. Journal of Physical Chemistry B. 1998; 102:8343–8346.

5. George SD, Metz M, Szilagyi RK, Wang HX, Cramer SP, Lu Y, Tolman WB, Hedman B, Hodgson KO, Solomon EI. Journal of the American Chemical Society. 2001; 123:5757–5767. [PubMed: 11403610]
6. George SJ, Lowery MD, Solomon EI, Cramer SP. Journal of the American Chemical Society. 1993; 115:2968–2969.
7. Bertini, I., Gray, B, JH., S, L., Valentine, JS. Bioinorganic Chemistry. University Science Books; Mill Valley, CA: 1994.
8. Albracht SPJ. Biochimica Et Biophysica Acta-Bioenergetics. 1994; 1188:167–204.
9. Cammack, R., Fernandez, VM., Hatchikian, EC. Inorganic Microbial Sulfur Metabolism. LeGall, J., Peck, HD., Jr, editors. Vol. 243. Academic Press Inc.; San Diego, CA: 1994. p. 43-67.
10. Pickering IJ, George GN, Lewandowski JT, Jacobson AJ. Journal of the American Chemical Society. 1993; 115:4137–4144.
11. Coyle, CL., Stiefel, EI. The Bioinorganic Chemistry of Nickel. Lancaster, JR., Jr, editor. VCH Publishers; New York: 1988. p. 1-28.
12. Wang H, Ralston CY, Patil DS, Jones RM, Gu W, Verhagen M, Adams MWW, Ge P, Riordan C, Marganian CA, Mascharak P, Kovacs J, Miller CG, Collins TJ, Brooker S, Croucher PD, Wang K, Stiefel EI, Cramer SP. Journal of the American Chemical Society. 2000; 122:10544–10552.
13. Wang HX, Peng G, Miller LM, Scheuring EM, George SJ, Chance MR, Cramer SP. Journal of the American Chemical Society. 1997; 119:4921–4928.
14. deGroot FMF. J. Electron Spec. Rel. Phen. 1994; 67:529–622.
15. Stohr, J. NEXAFS Spectroscopy. Springer-Verlag; New York, NY: 1992.
16. Stohr J, Nakajima R. IBM J. Res. Dev. 1998; 42:73–88.
17. Braun A, Bergmann U, Wang H, Gu W, Cramer SP, Tucker, Cairns EJ. Journal of Power Sources. 2003; 112:231–235.
18. Starace AF. Physical Review B. 1972; 5:1773–1784.
19. Thole BT, Carra P, Sette F, van der Laan G. Physical Review Letters. 1992; 68:1943–1946. [PubMed: 10045260]
20. O'Brien WL, Tonner BP. Physical Review B. 1994; 50:12672–12681.
21. Carra P, Thole BT, Altarelli M, Wang X. Physical Review Letters. 1993; 70:694–697. [PubMed: 10054179]
22. Zemva B, Chacon L, Lutar K, Shen C, Allman J, Bartlett N. Journal of Fluorine Chemistry. 1995; 71:195–196.
23. Mansour AN, Melendres CA. Physica B. 1995; 209:583–584.
24. Mansour AN, Melendres CA. Journal of Physical Chemistry A. 1998; 102:65–81.
25. Ge PH, Riordan CG, Yap GPA, Rheingold AL. Inorganic Chemistry. 1996; 35:5408–5409. [PubMed: 11666723]
26. Ram MS, Riordan CG, Ostrander R, Rheingold AL. Inorganic Chemistry. 1995; 34:5884–5892.
27. Hay M, Richards J, Lu Y. Proc. Natl. Acad. Sci. USA. 1996; 93:461–464. [PubMed: 8552661]
28. DeBeer S, Randall DW, Nersissian AM, Valentine JS, Hedman B, Hodgson KO, Solomon EI. Journal of Physical Chemistry B. 2000; 104:10814–10819.
29. George SD, Basumallick L, Szilagyi RK, Randall DW, Hill MG, Nersissian AM, Valentine JS, Hedman B, Hodgson KO, Solomon EI. Journal of the American Chemical Society. 2003; 125:11314–11328. [PubMed: 16220954]
30. Andreesen JR, Schaupp A, Neurater C, Brown A, Ljungdahl LG. J. Bacteriology. 1973; 114:743–751.
31. Ralston CY, Wang H, Ragsdale SW, Kumar M, Spangler NJ, Ludden PW, Gu W, Jones RM, Patil DS, Cramer SP. Journal of the American Chemical Society. 2000; 122:10553–10560.
32. He SH, Teixeira M, LeGall J, Patil DS, Moura I, Moura JJG, DerVartanian DV, Huynh BH, Peck HD Jr. Journal of Biological Chemistry. 1989; 264:2678–2682. [PubMed: 2536719]
33. Patil DS. Methods in Enzymology. 1994; 243:68–94. [PubMed: 7830621]
34. Tirsell KG, Karpenko VP. Nuclear Instruments & Methods In Physics Research Section A. 1990; 291:511–517.

35. Hussain Z, Huff WRA, Keller SA, Moler EJ, Heimann PA, McKinney W, Padmore HA, Fadley CS, Shirley DA. Journal of Electron Spectroscopy and Related Phenomena. 1996; 80:401–404.
36. Young AT, Arenholz E, Feng J, Padmore H, Marks S, Schlueter R, Hoyer E, Kelez N, Steier C. Surface Review and Letters. 2002; 9:549–554.
37. van Elp J, George SJ, Peng G, Searle BG, Zhou ZH, Adams MWW, Chen CT, Cramer SP. SPIE Proceedings. 1993; 2010:181–189.
38. le Grand JB, Mears CA, Hiller LJ, Frank M, Labov SE, Netel H, Chow D, Friedrich S, Lindeman MA, Barfknecht AT. Appl. Phys. Lett. 1998; 73:1295.
39. Friedrich S, Hiller LJ, Frank M, le Grand JB, Mears CA, Nideroest B, Labov SE, Barfknecht AT, LeGros M, Cramer SP. Journal of Electron Spectroscopy and Related Phenomena. 1999; 111:891–896.
40. Carpenter MH, Friedrich S, Hall JA, Harris J, Warburton WK, Cantor R. IEEE Transactions on Applied Superconductivity. 2013; 23:2400504–2400504.
41. Carpenter MH, Friedrich S, Hall JA, Harris J, Cantor R. Journal of Low Temperature Physics. 2014; 176:222–227.
42. Drury OB, Friedrich S. IEEE TRANSACTIONS ON APPLIED SUPERCONDUCTIVITY. 2005; 15:613.
43. Wang H, Yoda Y, Dong W, Huang SD. J. Synchrotron Rad. 2013; 20
44. Friedrich S, Drury OB, Cramer SP, Green PG. Nuclear Instruments and Methods in Physics Research A. 2006; 559:776–778.
45. Friedrich S, Funk T, Drury O, Labov SE, Cramer SP. Review of Scientific Instruments. 2002; 73:1629–1631.
46. CXRO. X-Ray Data Booklet. 2000. http://xdb.lbl.gov/Section1/Sec_1-1.html
47. Abe H, Niwa Y, Kitano M, Inoue Y, Yokoyama T, Hara M, Hosono H. Bulletin of the Chemical Society of Japan. 2017; 90:963–965.
48. Eriksson O, Johansson B, Albers RC, Boring AM, Brooks MSS. Phys. Rev.. B: Condens. Matter. 1990; 42:2707–2710. [PubMed: 9995756]
49. Soederlind P, Eriksson O, Johansson B, Albers RC, Boring AM. Phys. Rev.. B: Condens. Matter. 1992; 45:12911–12916. [PubMed: 10001354]
50. Bagus PS, Broer R, de Graaf C, Nieuwpoort WC. Journal of Electron Spectroscopy and Related Phenomena. 1999; 99:303–319.
51. Choisnet J, Evarestov RA, Tupitsyn II, Veryazov VA. Journal of Physics and Chemistry of Solids. 1996; 57:1839–1850.
52. Gu W, Wang H, Wang K. Dalton Transactions. 2014; 43:6406–6413. [PubMed: 24604143]
53. Cramer SP, Ralston CY, Wang HX, Bryant C. Journal of Electron Spectroscopy and Related Phenomena. 1997; 86:175–183.
54. Solomon EI, Baldwin MJ, Lowery MD. Chem. Rev. 1992; 92:521–542.
55. George SJ, Vanelp J, Chen J, Ma Y, Chen CT, Park JB, Adams MWW, Searle BG, Degroot FMF, Fuggle JC, Cramer SP. Journal of the American Chemical Society. 1992; 114:4426–4427.
56. Ralston CY, Wang HX, Ragsdale SW, Kumar M, Spangler NJ, Ludden PW, Gu W, Jones RM, Patil DS, Cramer SP. J. Am. Chem. Soc. 2000; 122:10553–10560.
57. Wang H, Patil DS, Ralston CY, Bryant C, Cramer SP. Journal of Electron Spectroscopy and Related Phenomena. 2001; 114:865–871.
58. Wang HX, Patil DS, Gu WW, Jacquamet L, Friedrich S, Funk T, Cramer SP. Journal of Electron Spectroscopy and Related Phenomena. 2001; 114:855–863.
59. Moura JJG, Teixeira M, Moura I. Pure. Appl. Chem. 1989; 61:915.
60. Ogata H, Lubitz W, Higuchi Y. Dalton Transactions. 2009; :7577–7587.doi: 10.1039/b903840j [PubMed: 19759926]
61. Bagyinka C, Whitehead JP, Maroney MJ. Journal of the American Chemical Society. 1993; 115:3576–3585.
62. Gu W, Wang H, Wang K. Journal of Synchrotron Radiation. 2015; 22:124–129. [PubMed: 25537598]

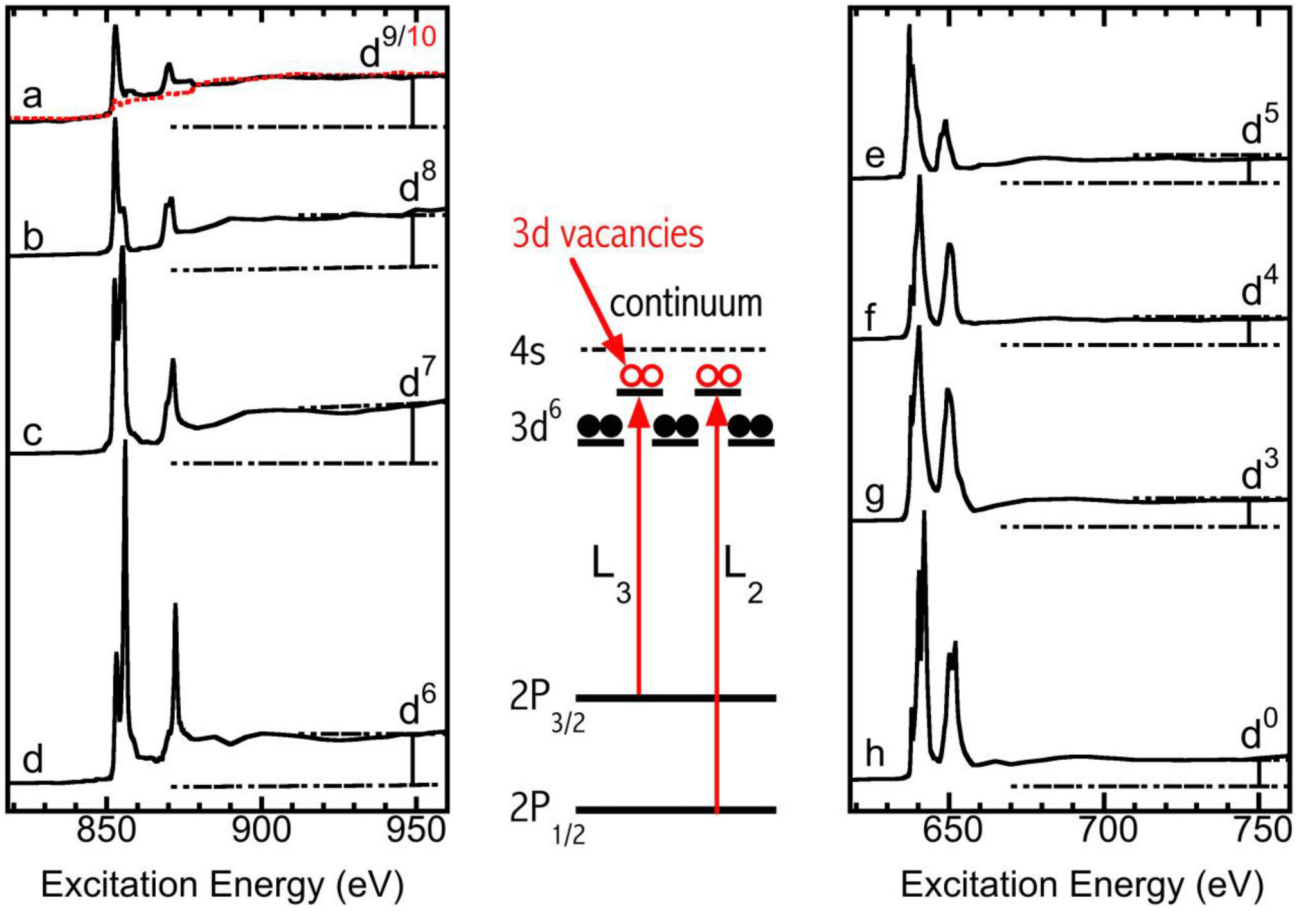

Figure 1.

Normalized L-edge XAS spectra. Left panel (from top to bottom): $Na_2[Ni^0(RS)_4]$ (a, dashed red line), $Na[Ni^I(RS)_4]$ (a, black line), $Ni^{II}O$ (b), $K_3Ni^{III}F_6$ (c), $KNi^{IV}IO_6$ (d); right panel (from top to bottom): $Mn^{II}O$ (e), $LiMn^{III}O_2$ (f), $Mn^{IV}O_2$ (g), $KMn^{VII}O4$ (h); the schematic energy diagram in the middle panel illustrates the 3d holes and the L_3 and L_2 (2p→3d) transitions.

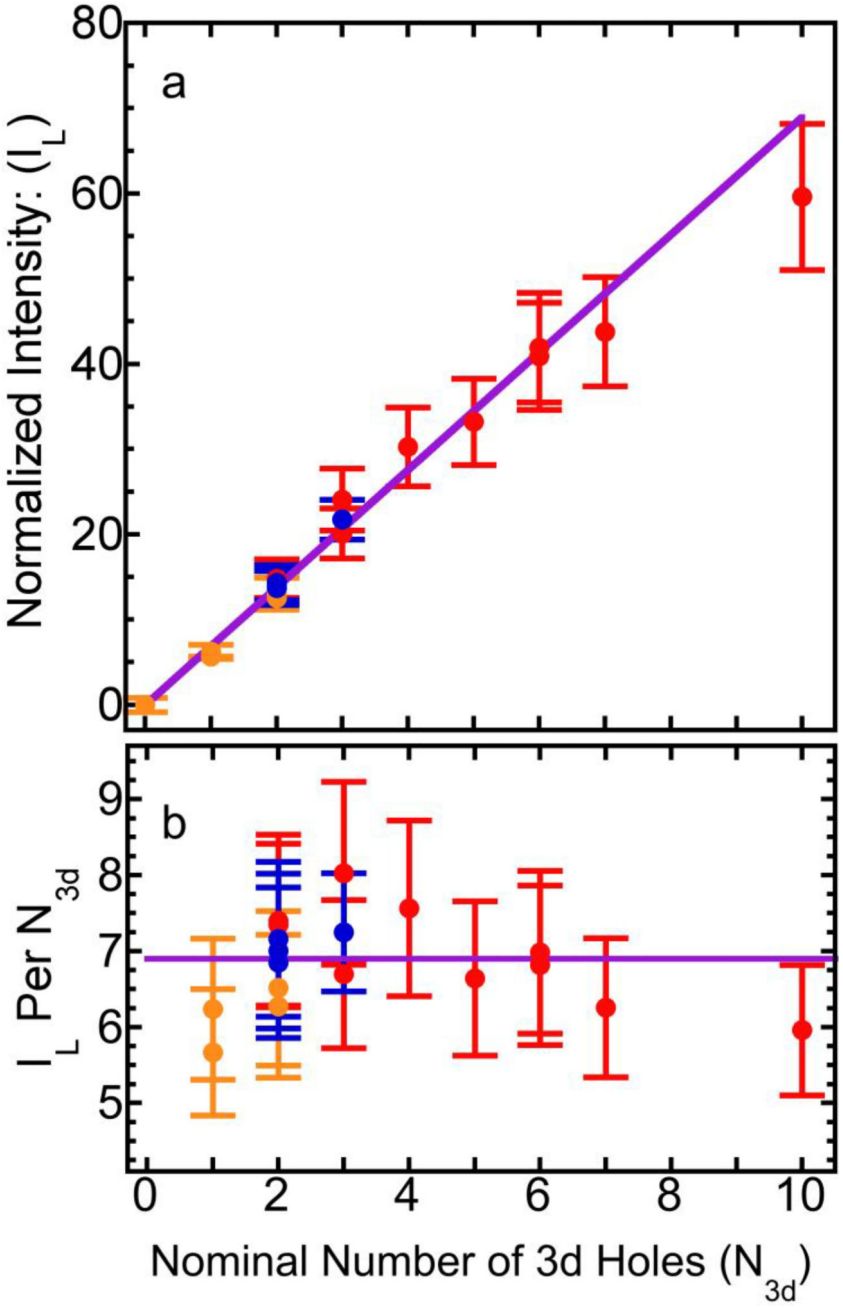

Figure 2.

(a) The integrated L-edge intensity I_L (= I_{L3}+I_{L2}) as a function of the nominal number of 3d holes (N_{3d}); (b) the I_L per nominal 3d hole (per N_{3d}) vs. nominal number of 3d holes (N_{3d}). The solid purple lines are the linear correlation functions for the data presented here.

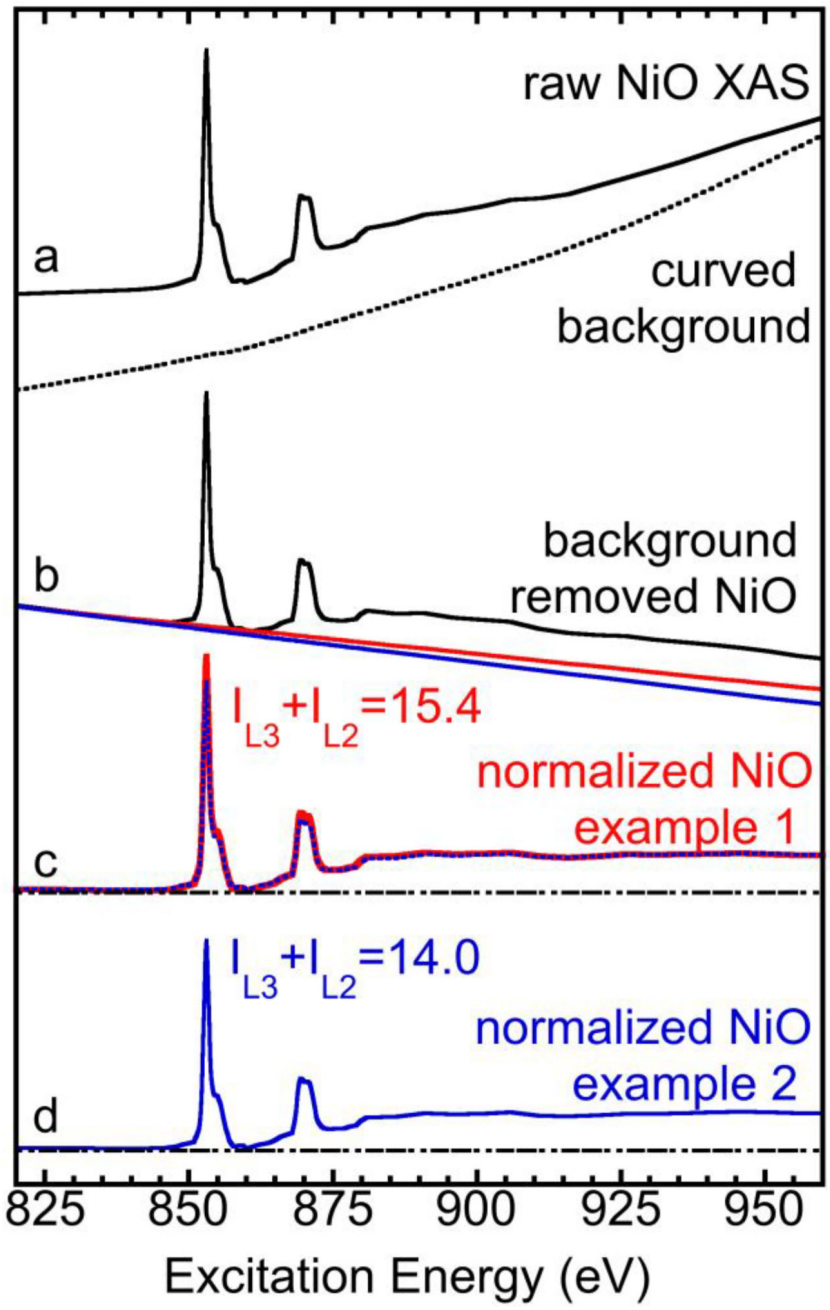

Figure 3.

(a) The measured raw NiO XAS (solid line) vs. the sample holder (as a background line reference) (dotted line); (b) NiO XAS with the background removed vs. the two possible new background slopes (blue and red); (c) NiO L XAS normalized with the example 1 processed baseline step (red) vs. the one normalized with example 2 processed baseline step (blue); (4) NiO L XAS normalized with example 2 processed baseline (blue).

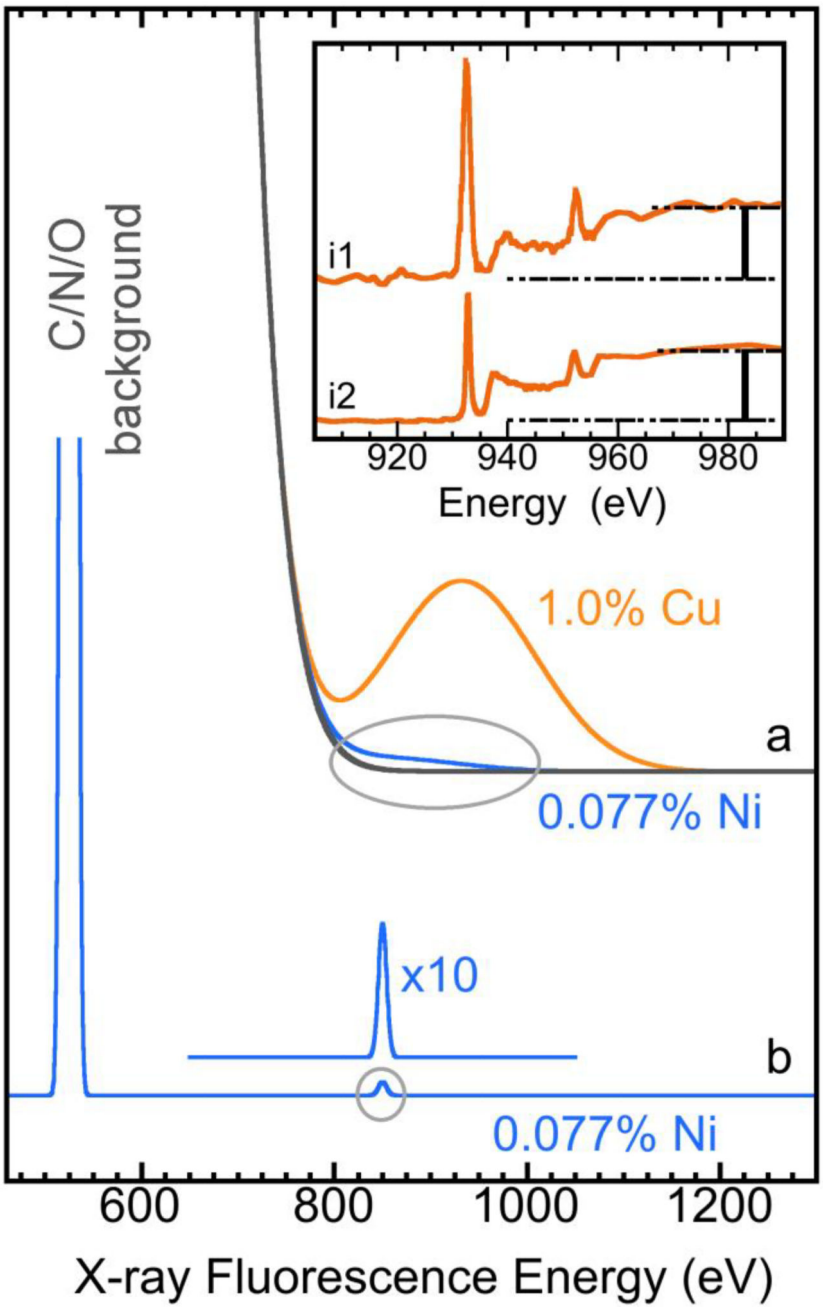

Figure 4.

An theoretical X-ray fluorescence spectrum for a hypothetical sample of 1% Cu and 0.077% Ni and O in balance: (a) measured with a 180 eV energy resolution X-ray fluorescence detector; or (b) measured with an STJ detector with 15 eV energy resolution; Inset: the normalized L XAS for Cu proteins from engineered *azurin* (i1)[5] and from *plastocyanin* (i2)[6] measured with a 180 eV Ge detector.

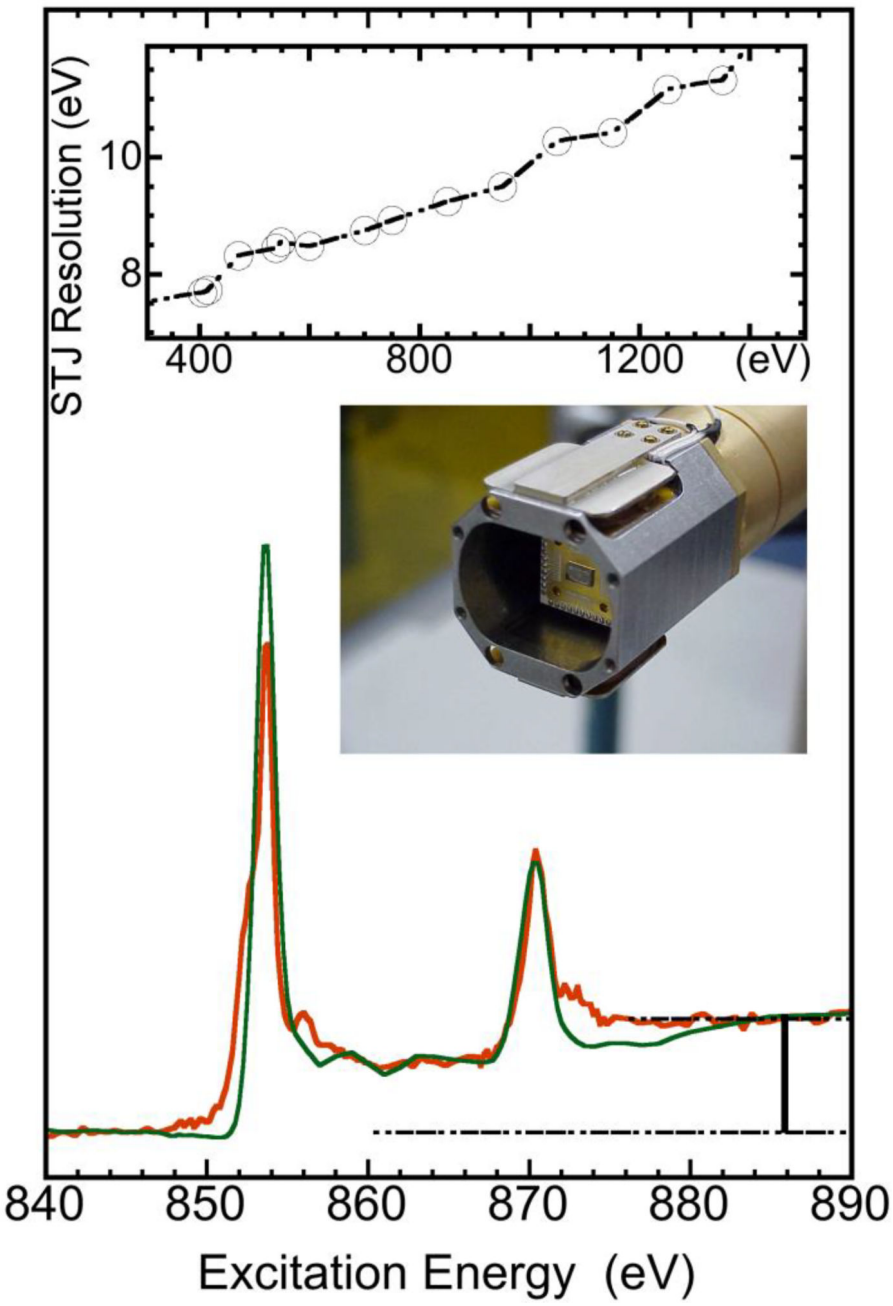

Figure 5.

Normalized L XAS for Ni inside a dilute *Ct*-CODH enzyme (<0.077% Ni) measured by partial fluorescence yield with an STJ detector (red) and inside a concentrated $[Ni^{II}(RS)_4]$ complex measured by total electron yield with a channeltron (green). The top inset shows the energy resolution in the region of 300–1500 eV for an advanced STJ detector. The middle inset is a photo of a STJ head snout.

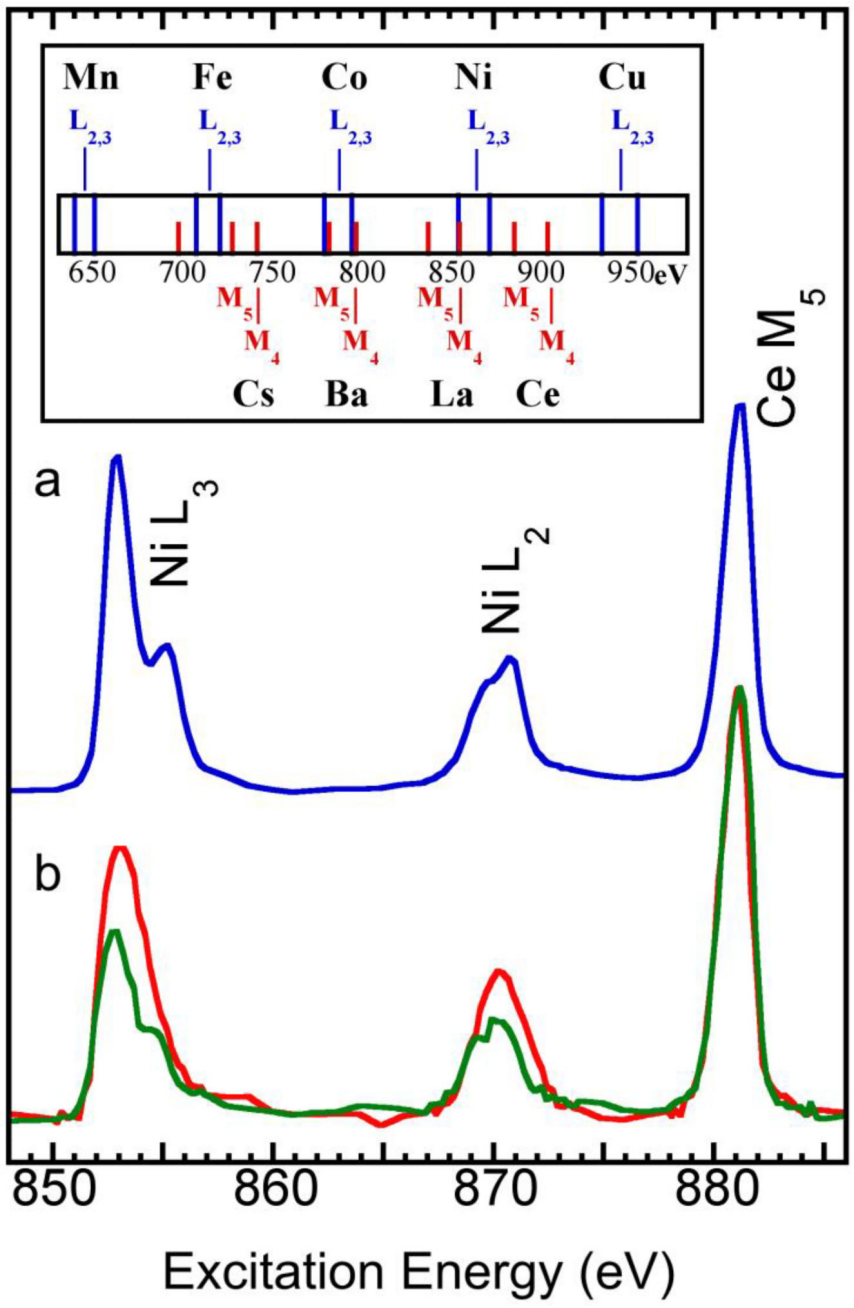

Figure 6.

Ni L XAS spectra for the 0.6% wt. Ni in a $NiBr_2$ matrix (a, blue), along with the as-isolated (b, red) and H_2-reduced (b, green) *D. gigas* NiFe H_2ase. All samples are doped with chemically-inert $Ce(NO_3)_3$. The top inset shows the M-edge positions for various rare earth elements in the region of 600–1000 eV.

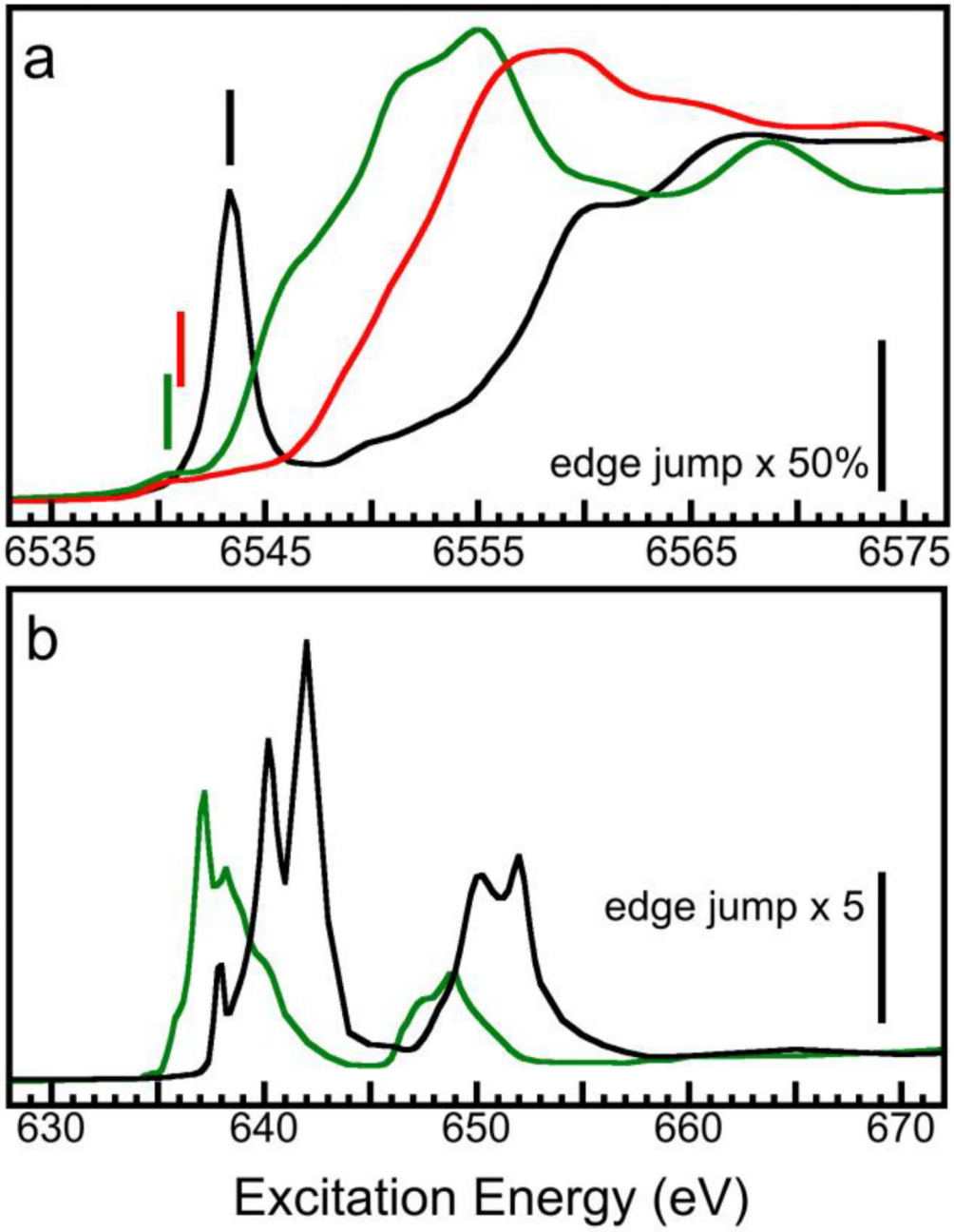

Figure 7.

(a) The K XAS for MnO (green), Mn_2O_3 (red) and $KMnO_4$ (black) in the pre-edge 1s→3d region; (b) the L XAS for MnO (green) and $KMnO_4$ (black).

Table 1

The integrated and normalized L intensities (I_L), edge jumps (J), L intensity derived number of 3d holes (H_{3d}) and their corresponding errors ($\delta\alpha$ and δ_{H3d}) for a series of Ni and Mn complexes with different ligand types.

Complex	d^N	Coord. Atom	I_L	J	$\alpha=I_L/J$	$\delta\alpha/\alpha$	$\delta\alpha$	Obs. H_{3d}	Obs. δ_{H3d}
$Na_2[Ni^0(SR)_4]$	d^{10}	S	0.00	1.01	0.00	--	--	0.00	--
$Na[Ni^I(SR)_4]$	d^9	S	5.39	0.95	5.67	0.107	0.61	0.66	0.071
$[PhTt^{tBu}]Ni^I(CO)$	d^9	S	6.43	1.03	6.24	0.109	0.68	0.73	0.079
$Ni^{II}Br_2$	d^8	Br	15.07	1.10	13.70	0.103	1.41	1.59	0.164
$Ni^{II}Cl_2$	d^8	Cl	14.29	1.02	14.01	0.105	1.48	1.63	0.172
$Ni^{II}F_2$	d^8	F	14.46	1.01	14.32	0.101	1.44	1.66	0.168
$Ni^{II}O$	d^8	O	16.02	1.09	14.70	0.105	1.54	1.71	0.179
$[Ni^{II}(SR)_4]$	d^8	S	11.55	0.92	12.55	0.112	1.41	1.46	0.164
$K_3Ni^{III}F_6$	d^7	F	25.05	1.04	24.09	0.111	2.68	2.80	0.312
$KNi^{IV}IO_6$	d^6	O	29.95	1.02	29.36	0.113	3.30	3.41	0.384
$Mn^{II}O$	d^5	O	34.60	0.94	36.81	0.115	4.24	4.28	0.493
$LiMn^{III}O_2$	d^4	O	41.50	0.99	41.92	0.116	4.87	4.87	0.566
$Mn^{III}_2O_3$	d^4	O	42.53	1.04	40.89	0.117	4.78	4.76	0.555
$Mn^{IV}O_2$	d^3	O	45.23	1.01	44.78	0.107	4.77	5.21	0.555
$KMn^{VII}O_4$	d^0	O	65.56	1.10	59.60	0.097	5.78	6.93	0.672